Journal of Nanobiotechnology

RESEARCH

Open Access

Selenium nanoparticles activate selenoproteins to mitigate septic lung injury through miR-20b-mediated RORγt/STAT3/Th17 axis inhibition and enhanced mitochondrial transfer in BMSCs

Wan-Jie Gu[1†], Feng-Zhi Zhao[1†], Wei Huang[1], Ming-Gao Zhu[1], Hai-Yan Huang[1], Hai-Yan Yin[1*] and Tianfeng Chen[1*]

Abstract

Sepsis-induced acute lung injury (ALI) remains a critical clinical challenge with complex inflammatory pathogenesis. While bone marrow mesenchymal stem cells (BMSCs) demonstrate therapeutic potential through anti-inflammatory and cytoprotective effects, their age-related functional decline limits clinical utility. This study developed chitosan-functionalized selenium nanoparticles (SeNPs@CS, 100 nm) to rejuvenate BMSCs through miR-20b-mediated selenoprotein biosynthesis. Mechanistic investigations revealed that SeNPs@CS-treated BMSCs exhibited enhanced mitochondrial transfer capacity, delivering functional mitochondria to damaged alveolar epithelial cells (AECII) for cellular repair. Concurrently, miR-20b upregulation suppressed the RORγt/STAT3/Th17 axis, reducing pro-inflammatory Th17 cell differentiation in $CD4^+$ T lymphocytes. The dual-target mechanism integrates immunomodulation via Th17 pathway inhibition with mitochondrial rejuvenation therapy, representing a paradigm-shifting approach for ALI management. These engineered BMSCs mitigated inflammatory markers in murine models, demonstrating superior efficacy to conventional BMSC therapies. Our findings establish SeNPs@CS-modified BMSCs as a novel therapeutic platform combining nanotechnology-enhanced stem cell engineering with precision immunometabolic regulation, providing new avenues for the treatment of sepsis-induced ALI.

Keywords Selenium, Acute lung injury, BMSCs, RORγt/STAT3, Th17, Mitochondrial transfer

†Wan-Jie Gu and Feng-Zhi Zhao contributed equally to this work.

*Correspondence:
Hai-Yan Yin
haiyanyin1867@126.com
Tianfeng Chen
tchentf@jnu.edu.cn
[1]Department of Intensive Care Unit, The First Affiliated Hospital, Department of Chemistry, State Key Laboratory of Bioactive Molecules and Druggability Assessment, MOE Key Laboratory of Viral Pathogenesis & Infection Prevention and Control, Jinan University, Guangzhou, China

Introduction

Sepsis, as a severe infectious disease, continues to exhibit high morbidity and mortality rates [1, 2] According to statistics, there are over 19 million cases of severe sepsis worldwide each year. Research has found that sepsis can trigger an inflammatory response, leading to uncontrolled inflammation [3, 4]. Persistently high levels of inflammation can result in systemic inflammatory response syndrome (SIRS), which may further induce multiple organ dysfunction. As a critical site for oxygenation and gas exchange in the body, the lungs are highly susceptible to the effects of sepsis [5]. Clinical studies have shown that sepsis-induced acute lung injury (ALI) is one of the most common complications among patients in intensive care units [6]. When the body suffers from severe infection, a large number of inflammatory cells are recruited and activated in the lung tissue, disrupting the alveolar epithelial barrier. This allows cytotoxic substances such as microbial particles, necrotic cells, and their contents to penetrate the barrier and enter the alveolar space, leading to an imbalance in the ventilation-perfusion ratio, hypoxemia, and decreased lung compliance. Concurrently, Th17 levels in peripheral blood and bronchoalveolar lavage fluid rise sharply, ultimately resulting in patient death due to severe and irreversible respiratory failure and infection [7, 8]. Numerous studies have indicated that mitochondrial dysfunction is a key factor in the pathogenesis of ALI [9, 10]. Mitochondria, as the core sites of cellular energy metabolism and important redox centers, are significantly affected by increased inflammatory cytokines and oxidative stress during the acute phase of ALI. This dysfunction leads to reduced ATP production, decreased mitochondrial membrane potential, diminished mitochondrial energy metabolism (OCR), and excessive inflammation, thereby causing mitochondrial damage and exacerbating lung tissue injury [11–13] Therefore, elevated Th17 levels, mitochondrial dysfunction, and inflammatory responses are closely associated with the development of ALI. Inhibiting Th17 expression, reducing inflammation, and delivering healthy mitochondria to the site of lung injury are crucial for repairing and treating ALI.

Currently, there is no reliable clinical treatment for ALI, with supportive care being the primary approach. Multidisciplinary collaboration is employed to achieve therapeutic goals through comprehensive strategies such as fluid managemen [14], glucocorticoid therapy [15], mechanical ventilation [16], immunomodulation [17], and nutritional support [18]. However, some commonly used treatments, such as mechanical ventilation and restrictive fluid management, may introduce additional side effects. For instance, mechanical ventilation can exacerbate lung injury [19], while restrictive fluid management may lead to hypotension and inadequate organ perfusion. Moreover, the misuse of glucocorticoids can disrupt the immune system, increasing the risk of infections and other complications. With advancements in technology, the dual application of nanomaterials and cell therapy has been extensively studied in disease treatment and continues to demonstrate significant efficacy. Nanodrug delivery systems, for instance, can target ligands through surface modification, enabling the directed delivery of bone marrow mesenchymal stem cells (BMSCs) or therapeutic drugs to diseased sites. Additionally, nanomaterials can respond to the diseased microenvironment to release active ingredients. For example, reactive oxygen species (ROS) responsive selenium nanoparticles (SeNPs) release Se at inflamed sites to activate antioxidant proteins (such as glutathione peroxidase) in BMSCs and thereby reduce oxidative damage. Furthermore, BMSCs secrete anti-inflammatory factors like IL-10 to suppress excessive inflammatory responses, while nanomaterials can further modulate the Th17/Treg balance, enhancing immune homeostasis [20]. Moreover, naturally derived nanomaterials exhibit excellent biocompatibility, reducing the risk of immune rejection associated with allogeneic BMSC transplantation [21, 22]. In recent years, stem cell therapy has achieved a series of breakthroughs in medical research [23–26] Mesenchymal stem cells, a type of adult stem cell derived from the mesoderm, can be obtained from various tissues such as bone marrow, umbilical cord, adipose tissue, amniotic membrane, liver, brain, and kidney. Among these, BMSCs exhibit excellent immunomodulatory, antioxidant, antiapoptotic, and regenerative repair properties, which help alleviate inflammatory responses [27]. BMSCs also have a long history of clinical application with well-documented data. As research on BMSCs progresses, their potential in treating sepsis-induced acute lung injury through immunomodulation, regenerative repair, and antioxidant stress functions has garnered increasing attention. However, during in vitro expansion, BMSCs tend to lose their differentiation potential, with significantly reduced proliferative and differentiative capacities [28]. The limited cell extraction yield and potential cell division arrest further restrict their clinical application. The application of nanomaterials can address these limitations. Studies have shown that nanoparticles, due to their unique size and abundant surface active sites, often exhibit high catalytic efficiency [29, 30]. Additionally, nanomaterials can mimic the natural extracellular matrix, providing physical and biochemical cues to promote stem cell proliferation and differentiation, guiding them toward specific cell types, and synchronously regulating the processes of proliferation and differentiation [31, 32]. Therefore, developing small-sized, highly catalytically active nanomedicines has become a goal for scientists. Selenium is an essential trace element for the human body, known for enhancing

immune function and combating free radical damage [33]. Selenium deficiency can lead to reduced immunity and may trigger SIRS [34]. As a crucial component of the body's antioxidant system, selenium participates in the synthesis of selenoproteins, such as glutathione peroxidase (GPX) and thioredoxin reductase (TrxR) [35, 36]. These enzymes are crucial antioxidants that can scavenge ROS and protect cells from oxidative damage [37, 38]. Numerous studies have reported that selenium nanoparticles and selenoproteins play a critical role in inhibiting oxidative stress injury, reducing free radical-induced oxidative reactions, mitigating tissue damage, and suppressing oxidative stress-induced inflammation [39–41]. Other studies have shown that selenium also shows better treatment effects in various tumors [42–44]. Furthermore, some studies have shown that low concentrations of SeNPs can enhance the viability and osteogenic potential of human mesenchymal stem cells by activating the JNK/FOXO3 pathway, thereby treating osteoarthritis [45]. However, research on whether SeNPs can act synergistically to promote the proliferation and differentiation of aged BMSCs remains unclear. Additionally, the importance of these proteins for the proliferation, differentiation, and sustained functionality of BMSCs is yet to be determined, warranting further investigation into the underlying mechanisms.

Numerous studies have shown that the level of Th17 cells is significantly elevated in the peripheral blood and bronchoalveolar lavage fluid of patients with sepsis-induced ALI, accompanied by severe mitochondrial dysfunction [46]. Moreover, these levels are positively correlated with the severity of the disease. Retinoic acid-related orphan receptorγt (RORγt) is a specific transcription factor for Th17 cells and directly participates in their differentiation [47]. Research indicates that RORγt is closely associated with the activation of signaling pathways such as IL-6, IL-21, and IL-23, which can induce the expression of RORγt and further promote Th17 cell differentiation [48]. The signal transducer and activator of transcription 3 (STAT3) is another critical transcription factor activated through the JAK/STAT signaling pathway [49]. It directly binds to the promoter region of the RORγt gene, thereby upregulating its expression. STAT3 regulates Th17 cell differentiation by directly acting on RORγt and indirectly influencing the expression of effector molecules such as IL-17 A [50]. Therefore, inhibiting the expression of RORγt/STAT3 and reducing Th17 cell differentiation can achieve anti-inflammatory effects. On the other hand, delivering healthy mitochondria to the injured lung tissue can also mitigate apoptosis in alveolar type II epithelial cells, achieving a dual-target therapeutic approach. Although nano-selenium exhibits excellent properties in promoting the proliferation, differentiation, and anti-inflammatory effects of BMSCs, it also introduces new challenges, such as a short half-life and poor stability. Chitosan (CS), known for its good biocompatibility and molecular structure rich in functional groups like hydroxyl groups, can interact with the surface of nanodrugs, forming stable chemical bonds or physical adsorption layers. This interaction prevents nanodrugs from aggregating in aqueous solutions or physiological environments, thereby enhancing their dispersibility and stability [51]. In this study, we prepared chitosan-functionalized selenium nanoparticles (SeNPs@CS) to achieve the biological stability of SeNPs. After co-incubating SeNPs@CS with BMSCs, we found that they could rapidly promote the proliferation and differentiation of BMSCs. The underlying mechanism involves the upregulation of miR-20b expression in BMSCs, which facilitates the conversion of nano-selenium into functional selenoproteins. In vitro studies revealed that when BMSCs cultured with SeNPs@CS were co-cultured with alveolar epithelial cells, healthy mitochondria from BMSCs were transferred to damaged AECII cells. Further in vivo experiments demonstrated that the combined treatment of SeNPs@CS and BMSCs could downregulate Th17 expression by inhibiting the RORγt/STAT3 signaling axis through the upregulation of miR-20b, exerting anti-inflammatory effects and ultimately achieving a dual-target therapeutic outcome. Clearly, the cell therapy involving the co-incubation of BMSCs with SeNPs@CS holds significant potential for further development as an effective treatment for ALI, representing a promising candidate therapy (Scheme 1).

Results and discussion

Design and synthesis of SeNPs@CS

Firstly, we successfully synthesized chitosan-modified selenium nanoparticles, denoted as SeNPs@CS (Fig. 1). The morphology of SeNPs@CS is shown in Fig. 1A and B, revealing uniform spherical nanoparticles. TEM images indicate a particle size of approximately 100 nm. The particle size distribution of SeNPs@CS is presented in Fig. 1C, with an average particle size of (120 ± 0.56 nm), a PDI of 0.15, and a Zeta potential of (21 ± 1.65mV), demonstrating the uniformity of the synthesized nanoparticles. Compared to CS, the surface charge of the synthesized SeNPs@CS has decreased (Fig. 1D), maintaining good biocompatibility while reducing toxicity. As shown in Fig. 1E, CS has an absorption peak at 208 nm, whereas the peak shifts to the left after the synthesis of SeNPs@CS, indicating the formation of a new material. Compared to CS, the infrared spectrum of SeNPs@CS (Fig. 1F) reveals a shift in the hydroxyl peak from 3432.82 cm^{-1} to 3442.46 cm^{-1}. Based on these and other characterization results, it can be concluded that SeNPs@CS have been successfully prepared. The XPS characterization results of SeNPs@CS are shown in

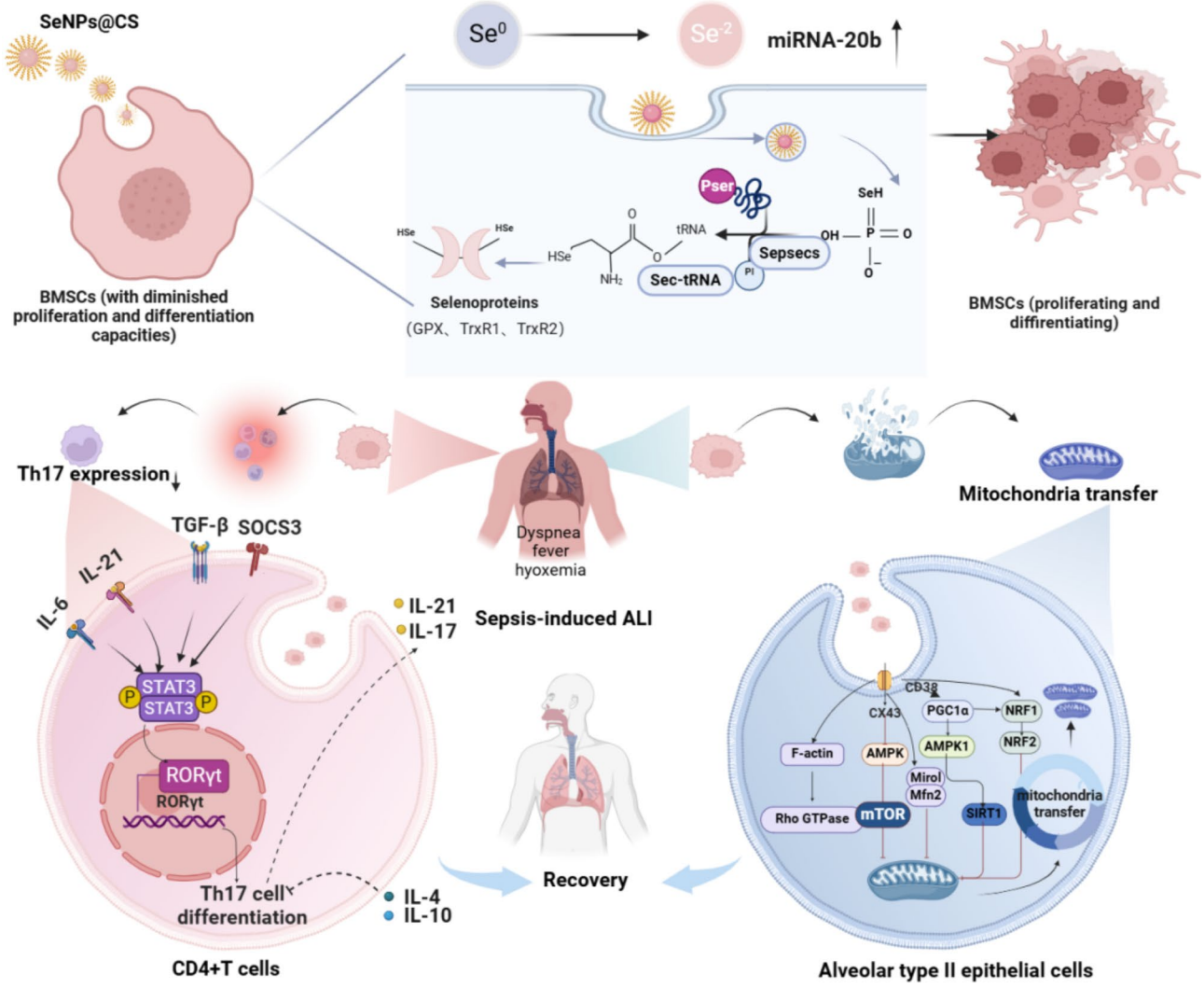

Scheme 1 Schematic illustration of SeNPs to mitigate septic lung injury through miR-20b-mediated RORγt/STAT3/Th17 axis inhibition and enhanced mitochondrial transfer in BMSCs

Fig. 1G, H, and I. According to the peak position of Se 3d in the selenium nanospectrogram (Fig. 1I), the presence of Se^0 is indicated in the sample near 54 eV (the highest peak among the Se peaks). No photometric intensity values were detected for the Se 2p, 2s, and 1s orbitals representing high-valent selenium, suggesting that Se^{4+} has been completely reduced by vitamin C. In summary, the above characterization experiments further confirm the successful preparation of SeNPs@CS.

SeNPs@CS promote BMSCs proliferation and differentiation by upregulating miR-20b

Further, we used SeNPs@CS to senescent BMSCs to investigate whether SeNPs@CS could promote the re-proliferation and differentiation of BMSCs and explore the underlying mechanisms. The experimental results are shown in Fig. 2A. Following the acquisition of the GSE9664 dataset from the GEO database, background correction and data normalization were performed, and DEGs were analyzed using the limma package. A total of eight differentially expressed miRNAs were identified, including three upregulated and five downregulated miRNAs. A volcano plot was used to visualize these differentially expressed miRNAs (Fig. S1). Additionally, hierarchical clustering was performed based on the expression levels of different miRNAs across samples, and a heatmap was generated to illustrate the expression patterns in different samples (Fig. S2). Notably, miR-20b was significantly downregulated in senescent BMSCs, suggesting a potential role in aged BMSC. CCK-8 was used to detect the proliferation of BMSCs (Fig. 2B). As the concentration of SeNPs@CS gradually increased, the proliferation activity of cells treated with 5 μM SeNPs@CS significantly increased compared to untreated BMSCs. The proliferation activity further increased at 10 μM and reached its peak at 20 μM and 40

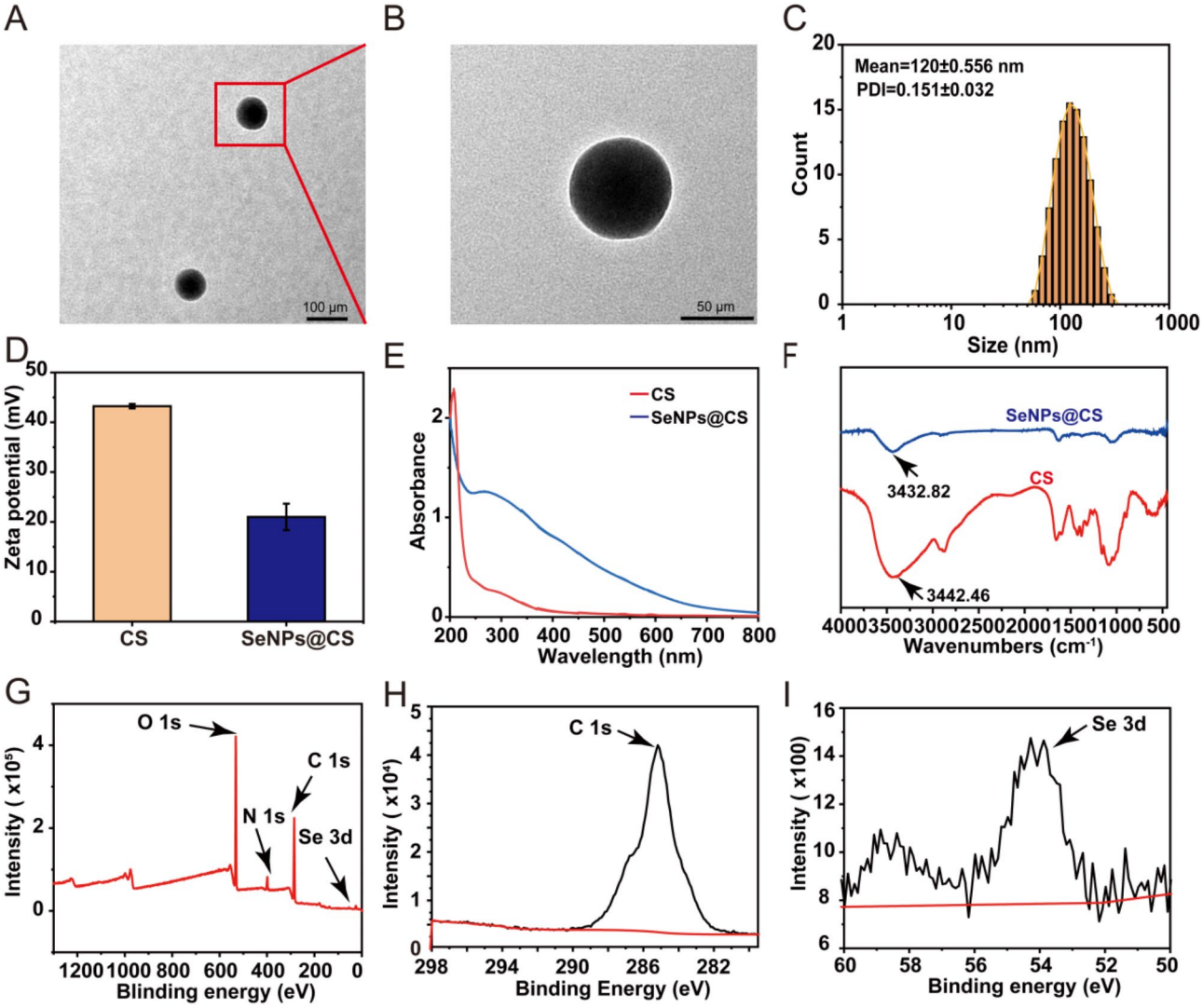

Fig. 1 Characterization of SeNPs@CS. (**A**, **B**) Representative TEM; (**A**) Images of SeNPs@CS. (**C**) Particle size distribution of SeNPs@CS. (**D**) Zeta potential of CS and SeNPs@CS. (**E**) UV spectra of CS and Se@CS NPs. (**F**) IR spectra of CS and SeNPs@CS. (**G**-**I**) XPS spectra of SeNPs@CS: (**G**) Survey spectrum, (**H**) C 1s spectrum, and (**I**) Se 3d spectrum

μM. Subsequently, real-time quantitative PCR (q-PCR) was employed to detect the expression of miRNA-20b (Fig. 2C). Compared to 0 μM, the expression of miRNA-20b significantly increased at 5 μM, further increased at 10 μM, and peaked at 20 μM and 40 μM. Next, mitochondrial function in BMSCs was assessed. The results of ATP and OCR tests are shown in Fig. 2D and E, respectively, with mitochondrial energy reaching its highest levels at 20 μM and 40 μM. We further used flow cytometry to detect the expression of CD44, CD105, and CD29 to verify the proliferation and differentiation of BMSCs (Fig. 2F, G, H, and I). Compared to 0 μM, the expression of CD44, CD105, and CD29 significantly increased at 5 μM, further increased at 10 μM, and peaked at 20 μM and 40 μM. Additionally, mitochondrial membrane potential, Ca^{2+} content, and mitochondrial count (Fig. 2J, K, L, M, N, and O) further validated the above results. These experimental results suggest that SeNPs@CS can promote the re-proliferation and differentiation of BMSCs by upregulating the expression of miRNA-20b and enhancing mitochondrial function.

Research indicates that selenium (Se), an indispensable non-metallic trace element in humans and animals, plays a profound role in maintaining health. As a critical component of the human antioxidant system, selenium participates in the synthesis of selenoproteins, the most common of which are glutathione peroxidase and thioredoxin reductase. The results show that, GPX is the most abundant selenoprotein in mammalian bodies. GPX could bind with four Se atoms, forming the active center of the enzyme molecule and thereby exerting its function. Changes in Se content directly affect the enzyme's

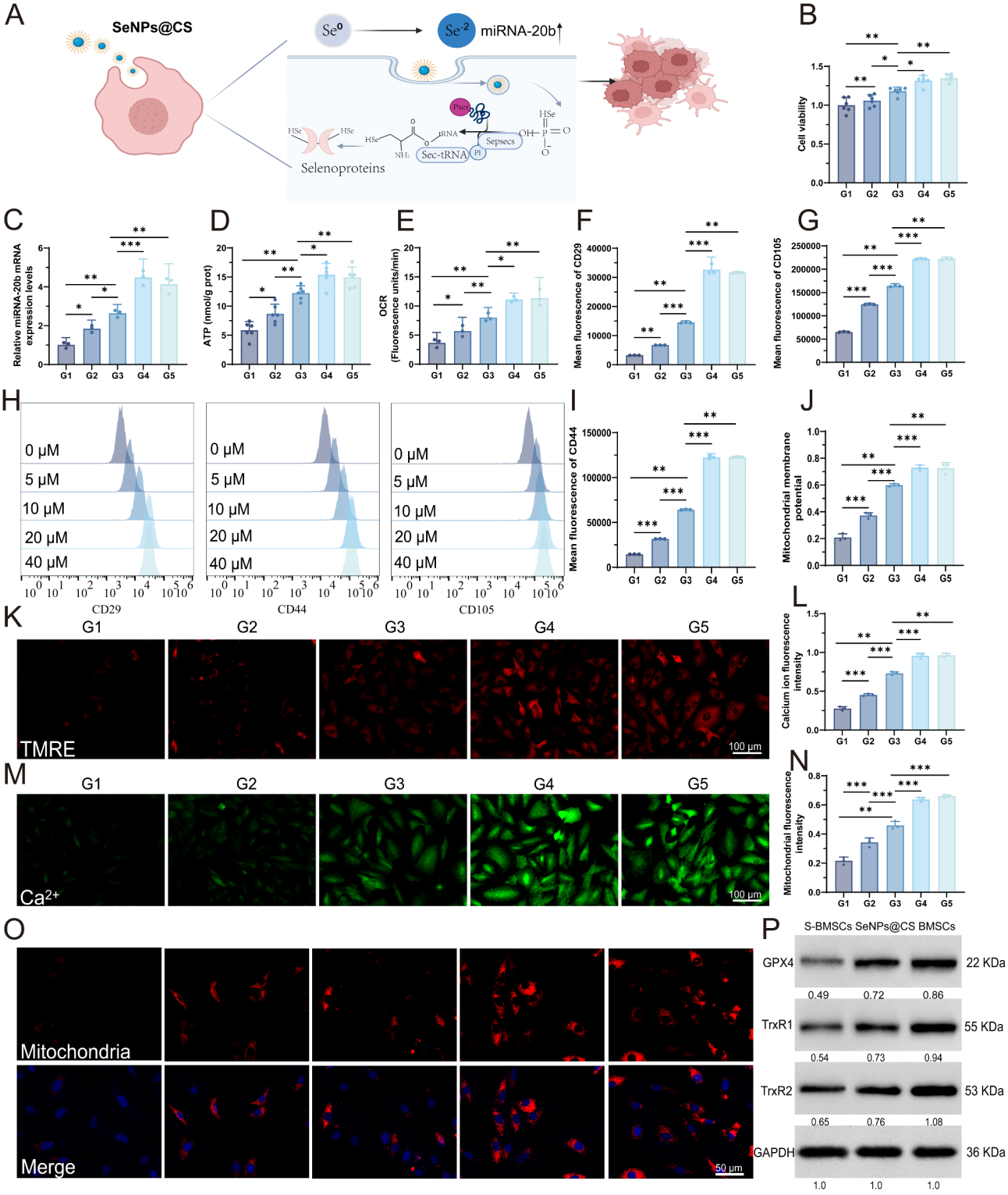

Fig. 2 (**A**) Mechanistic studies on the promotion of BMSCs proliferation and differentiation by SeNPs@CS. (**B**) Detection of BMSCs proliferation using CCK-8 assay. (**C**) q-PCR analysis for the expression of miRNA-20b. (**D**) Determination of mitochondrial ATP content. (**E**) Measurement of mitochondrial OCR content. (**F**, **G**, **H**, **I**) Flow cytometry analysis for BMSCs markers CD44, CD105, and CD29. (**J**, **K**) Determination of mitochondrial membrane potential. (**L**, **M**) Detection of mitochondrial Ca^{2+} content. (**N**, **O**) Quantification of mitochondrial number. (**P**) Western blot analysis for the expression of selenium-containing proteins GPX4, TrxR1, and TrxR2. G1: Control; G2: SeNPs@CS 5 μM; G3: SeNPs@CS 10 μM; G4: SeNPs@CS 20 μM; G5: SeNPs@CS 40 μM. ***($P < 0.001$), **($P < 0.01$), *($P < 0.05$)

activity, hence GPX is also known as a Se -dependent enzyme. Thioredoxin reductase (TrxR) is mainly found in the cytoplasm, mitochondria, liver, etc. This enzyme exhibits multiple biological activities, including regulating the body's redox state, defending against oxidative damage, modulating cell growth and proliferation, participating in signal transduction, and regulating immune responses. Studies have also shown that GPX and TrxR family proteins played pivotal roles in suppressing oxidative stress and maintaining redox homeostasis [52, 53]. The experimental results are shown in Fig. S3. q-PCR was used to detect glutathione peroxidase GPX (GPX-1, GPX-2, GPX-3, GPX-4, GPX-6) and thioredoxin reductase (TrxR1, TrxR2). The expression levels of GPX and TrxR families in senescent BMSCs induced by hydrogen peroxide (H_2O_2) were significantly lower than those in the normal BMSCs group. However, after treatment with SeNPs@CS, the expression levels of GPX and TrxR families increased significantly and partially recovered. Subsequently, Western blotting (WB) was used to detect the major proteins of GPX and TrxR (GPX4, TrxR1, and TrxR2) in each group. As shown in Fig. 2P, the expression of GPX4, TrxR1, and TrxR2 in the senescent BMSCs group was significantly lower than in the normal BMSCs group. However, after a certain amount of SeNPs@CS intervention, the expression levels of GPX4, TrxR1, and TrxR2 were alleviated. These results further demonstrate that SeNPs@CS can promote the transformation of nanoselenium into functional selenoproteins by upregulating the expression of miR-20b in senescent BMSCs, thereby accelerating mitochondrial respiration to generate energy and achieving rapid proliferation of BMSCs.

SeNPs@CS upregulates the expression of miR-20b in BMSCs, thereby targeting and inhibiting the RORγt/STAT3 pathway to downregulate Th17

Clinical studies have shown that the expression of Th17 is elevated in the peripheral blood and bronchoalveolar lavage fluid of ALI patients, which is closely associated with disease severity, inflammation levels, and poor prognosis. As a subset of pro-inflammatory T cells, Th17 cells exacerbate lung injury by secreting pro-inflammatory cytokines such as IL-17 and participating in inflammatory responses. Generally, RORγt and STAT3 play collaborative action in the differentiation of Th17 cells. STAT3 drives Th17 cell differentiation by activating RORγt expression and maintains Th17 cell function by regulating key factors such as IL-17 A. To validate that miRNA-20b can target and regulate the RORγt/STAT3 signaling pathway, thereby further inhibiting Th17 expression and reducing inflammation levels (Fig. 3A), We conducted a preliminary target prediction using various databases (Fig. S4 and Fig. 3B). In this study, multiple bioinformatics tools were employed to predict and screen the potential target genes of miR-20b. Specifically, TargetScan, miRDB, miRWalk, and DIANA-microT-CDS were used to predict genes that may be regulated by miR-20b. The prediction results from the four databases were then subjected to cross-analysis to enhance reliability and specificity, ultimately identifying 305 candidate target genes. To visually represent the screening results, a Venn diagram was constructed to illustrate the overlap among the databases. We utilized TargetScan, miRDB, miRWalk, and DIANA-microT-CDS to predict the potential target genes of miR-20b. Through cross-analysis, 305 common target genes were identified, and a Venn diagram was constructed for visualization. The results indicated that STAT3 is a key downstream target gene directly regulated by miR-20b. During Th17 cell differentiation, STAT3 functions as a core transcription factor whose activation promotes the expression of RORγt, a signature transcription factor of Th17 cells, thereby driving Th17 cell differentiation and functional maturation. Venn diagram illustrates the overlapping target genes of miR-20b predicted by multiple bioinformatics databases, including TargetScan, miRDB, miRWalk, and DIANA-microT-CDS. The intersecting region represents the common target genes identified across all databases. RNAhybrid predicts one binding site for hsa-miR-20b-5p with STAT3, and similarly, one binding site for hsa-miR-20b-3p with STAT3. In summary, the binding possibility between hsa-miR-20b-5p and STAT3 is the highest. We employed a dual-luciferase reporter assay to further investigate to detect the binding site between them. Figure 3A, B, and C demonstrated a significant decrease in fluorescence values in both groups after transfection with the miRNA-20b mimic. However, when the STAT3 sites were mutated, the fluorescence values did not change significantly after transfection with the miRNA-20b mimic, indicating the presence of binding sites. We further isolated and cultured $CD4^+$ T cells from C57BL/6J mice, identified and screened them using immunomagnetic beads and flow cytometry, and constructed OE-miRNA-20b BMSCs and OE-RORγt $CD4^+$ T cell models for co-culture. As shown in Fig. 3D, E, F, and G, flow cytometry was used to detect Th17 cell markers: IL-17 A^+ $CD4^+$ CD196 $(CCR6)^+$ and RORγt. The experimental results indicated that Th17 differentiation increased after treatment with OE-RORγt $CD4^+$ T cells. However, when co-cultured with normal BMSCs or OE-miRNA-20b BMSCs, the markers of Th17 differentiation significantly decreased. Moreover, when OE-miRNA-20b BMSCs incubated with SeNPs@CS were co-cultured with OE-RORγt $CD4^+$ T cells, the degree of Th17 differentiation was the lowest. Additionally, we used ELISA to detect the expression of pro-inflammatory cytokines (TGF-β, IL-17, IL-6, IL-21, Socs3) and anti-inflammatory cytokines (IL-2, IL-4, IL-10). Figure 3H, I, J, K, L, M, N, and O demonstrated that compared to the groups

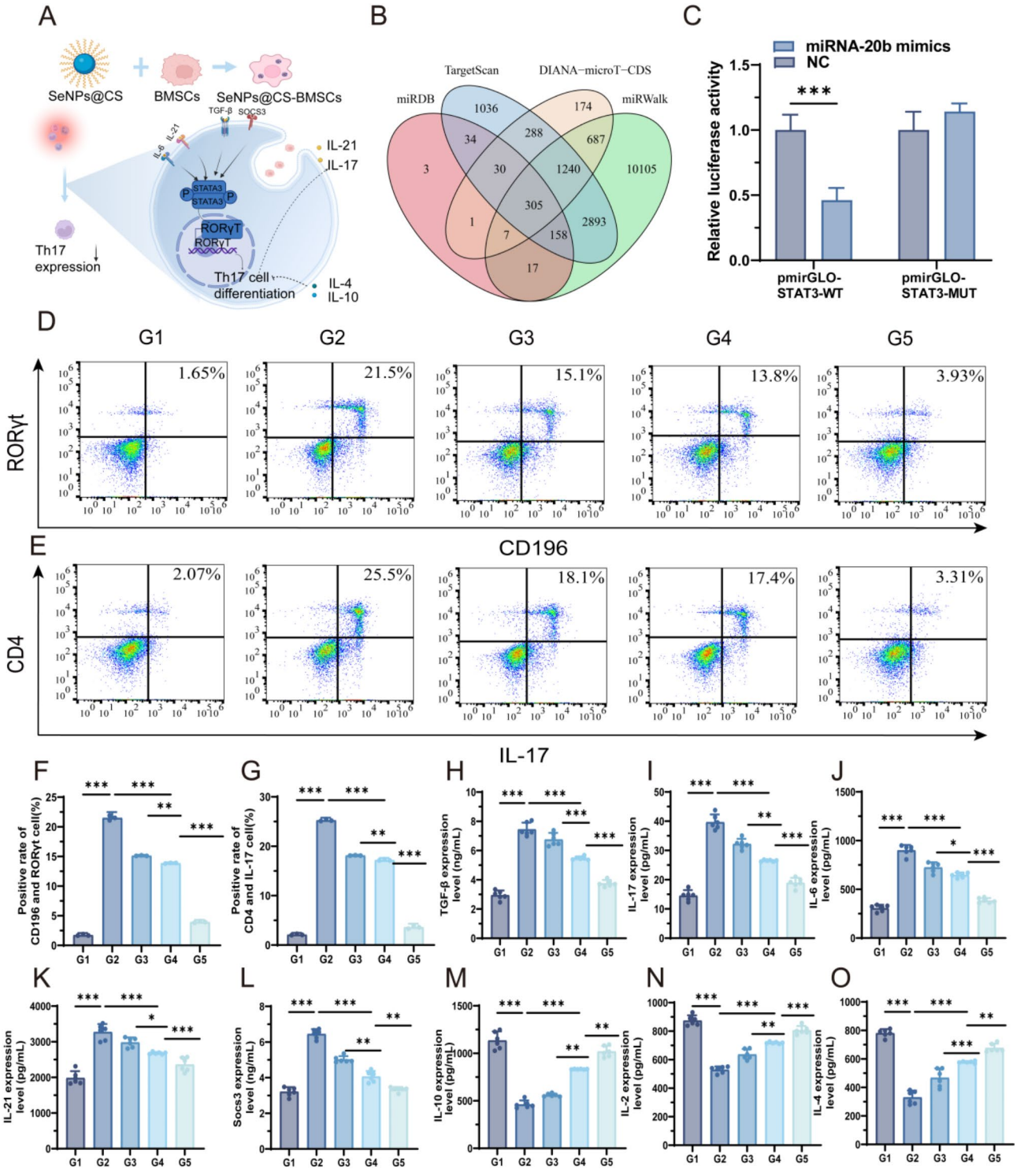

Fig. 3 Bioinformatic analysis of the targeting relationship between miRNA-20b and RORγt/STAT3 and their inflammatory levels. (**A**) Schematic diagram of the miRNA-20b and RORγt/STAT3 pathway. (**B**) Venn diagram representation. (**C**) Dual-luciferase reporter gene assay for miRNA-20b and STAT3. (**D**, **E**, **F**, **G**) Qualitative and quantitative analysis of Th17 cell markers in different groups. (**H**, **I**, **J**, **K**, **L**, **M**, **N**, **O**) Expression levels of TGF-β, IL-17, IL-6, IL-21, Socs3, IL-10, IL-2, and IL-4. G1: CD4 + T; G2: OE-RORγtCD4 + T; G3: BMSCs + RORγtCD4 + T; G4: OE-miRNA-20b-BMSCs + OE-RORγtCD4 + T; G5: SeNPs@CS + OE-miRNA-20b-BMSCs + OE-RORγt CD4 + T. ***($P < 0.001$), **($P < 0.01$), *($P < 0.05$)

co-cultured with normal BMSCs or OE-miRNA-20b BMSCs, the expression of pro-inflammatory cytokines increased, while the expression of anti-inflammatory cytokines decreased in the OE-RORγt $CD4^+$ T cell group. When OE-miRNA-20b MSCs incubated with SeNPs@CS were co-cultured with OE-RORγt $CD4^+$ T cells, the levels of pro-inflammatory cytokines were the lowest. These findings further indicate that BMSCs incubated with SeNPs@CS can inhibit the activation of the RORγt/STAT3 signaling pathway by upregulating the expression of miR-20b, further suppressing the differentiation of $CD4^+$ T cells into Th17 cells and ultimately exerting an anti-inflammatory effect.

SeNPs@CS upregulates the expression of miR-20b in BMSCs and conveys healthy mitochondria to injured lung epithelial cells AECII

Mitochondria, as the structures responsible for energy production in cells and the primary site for cellular aerobic respiration, play a profound role in processes such as cell proliferation, apoptosis, and differentiation. In recent years, it has been discovered that mitochondrial dysfunction plays a significant role in the process of ALI. To further validate the effectiveness of SeNPs@CS in synergy with BMSCs to promote the transfer of mitochondria to damaged lung epithelial cells, we constructed a co-culture model of BMSCs and AECII cells. The experimental results are shown in Fig. 4. Initially, we examined mitochondrial membrane potential and calcium ion content. As depicted in Fig. 4A and D, after induction with LPS, AECII cells experienced severe mitochondrial damage. However, upon co-culture with BMSCs, there was a recovery in mitochondrial membrane potential and calcium ion content, indicating that BMSCs can facilitate the restoration of AECII mitochondrial function. Compared to the BMSCs group, the OE-miR-20b-BMSCs co-culture group demonstrated significantly higher mitochondrial membrane potential and calcium ion content. Moreover, compared to the OE-miR-20b-BMSCs group, the OE-miR-20b-BMSCs group synergized with SeNPs@CS showed the highest mitochondrial membrane potential and calcium ion content. Figure 4B and E provide quantitative analysis results for Fig. 4A and D, respectively. Flow cytometry was further employed to assess cell apoptosis, and the results are presented in Fig. 4G and H. Following LPS intervention, apoptosis of AECII cells increased significantly. However, after co-culture with BMSCs, OE-miR-20b-BMSCs, or OE-miR-20b-BMSCs synergized with SeNPs@CS, the degree of apoptosis decreased notably. Mitochondrial ATP, OCR, and NAD^+ are crucial indicators of cellular energy metabolism and function. To further investigate mitochondrial recovery, we used ELISA kits to detect the expression of these three markers. The results, as shown in Fig. 4C, F, and I, reveal that after LPS intervention, mitochondrial function in AECII cells declined significantly. However, upon co-culture with BMSCs, OE-miR-20b-BMSCs, or OE-miR-20b-BMSCs synergized with SeNPs@CS, there was a restoration in mitochondrial function. Finally, transmission electron microscopy (TEM) was used to examine the mitochondrial structure, and the results are displayed in Fig. 4J. After LPS intervention, AECII cell mitochondria were damaged, exhibiting cristae rupture and vacuolization. However, after co-culture with BMSCs, OE-miR-20b-BMSCs, or OE-miR-20b-BMSCs synergized with SeNPs@CS, there was a recovery in mitochondrial structure. The mitochondria were enclosed by a double membrane, with a smooth outer membrane and an inner membrane protruding inwardly to form "cristae." These experimental results indicate that bone marrow mesenchymal stem cells incubated with SeNPs@CS exhibit strong repair-promoting capabilities, delivering healthy mitochondria to damaged cells, thereby improving mitochondrial injury in AEC II cells.

SeNPs@CS synergizes with BMSCs to achieve mitochondrial transfer to damaged lung epithelial cells AECII

To further verify the mitochondrial transfer, we conducted tests on mitochondrial transfer-related genes, proteins, and exchange rates (Fig. 5A). Cx43 is a profound mitochondrial transfer-related protein that mediates the intercellular transfer of mitochondria through gap junction channels. PGC1α is a nuclear receptor coactivator widely involved in mitochondrial biosynthesis and energy metabolism. Miro1, one of the key regulators of mitochondrial transfer, recruits actin and promotes mitochondrial transport along microtubules through interaction with TRAK1/2. Using q-PCR and WB for detection, experimental results (Fig. 5B, C, D, E, F, G, H, I, J, K, and L) demonstrate significantly enhanced mitochondrial transfer after LPS-induced AECII cells were co-cultured with BMSCs, OE-miR20b-BMSCs, or SeNPs@CS synergized OE-miR-20b-BMSCs. Flow cytometry was further employed for quantitative analysis of the mitochondrial exchange rate between BMSCs and AECII. As shown in Fig. 5M and N, compared to the BMSCs co-culture group, the mitochondrial exchange rate was notably elevated in the OE-miR-20b-BMSCs group. Moreover, the mitochondrial exchange rate was highest in the SeNPs@CS synergized OE-miR-20b-BMSCs group, indicating that BMSCs incubated with SeNPs@CS exhibit remarkable mitochondrial transfer capability, effectively transferring healthy mitochondria to damaged AECII cells. Furthermore, these results suggest that after co-culturing BMSCs with damaged AECII, mitochondrial transfer-related proteins such as Cx43, PGC1α, Miro1, CD38, and F-actin are significantly

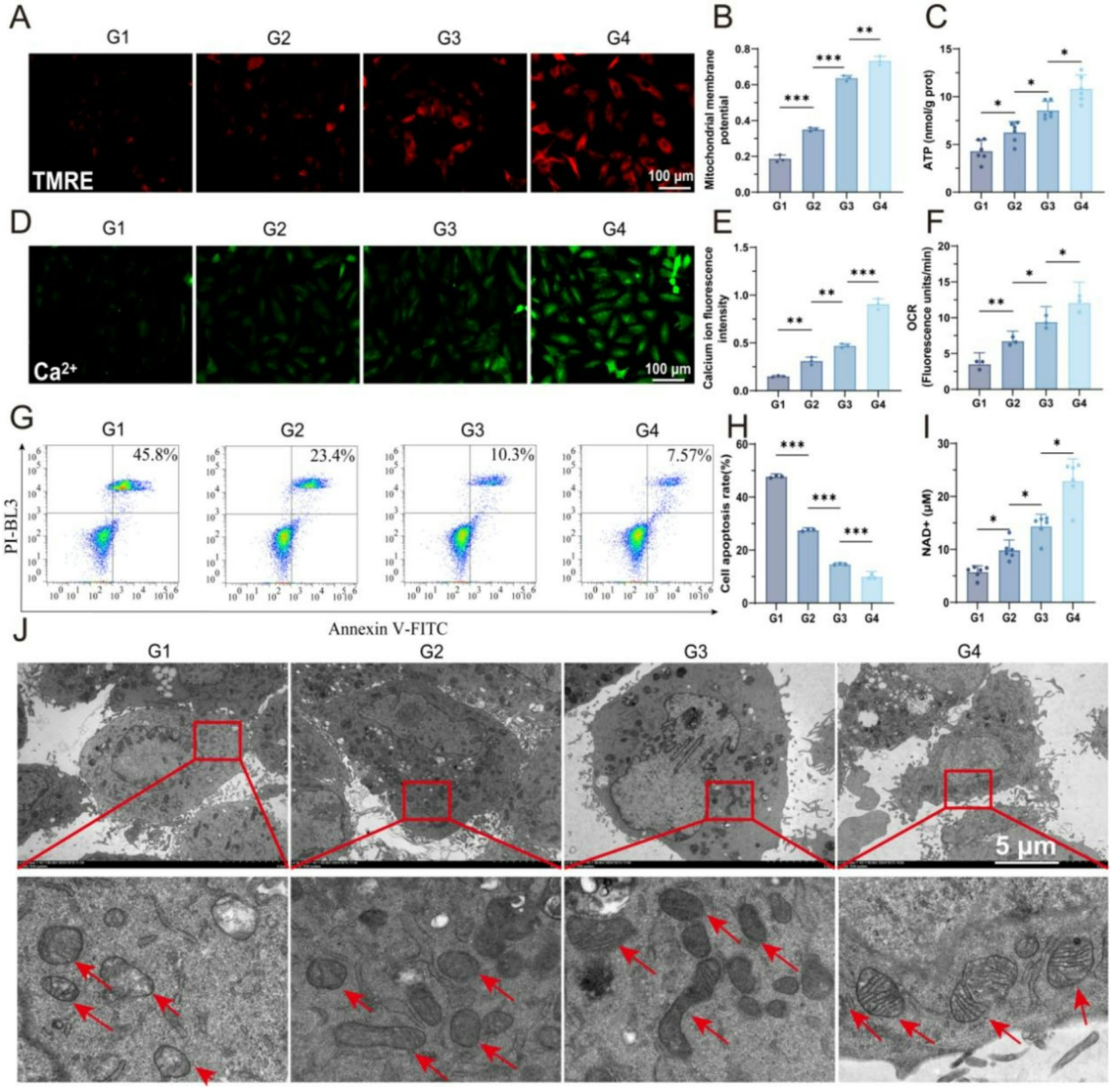

Fig. 4 SeNPs@CS synergizes with BMSCs to promote mitochondrial repair in damaged AECII cells. (**A**, **B**) Qualitative and quantitative detection of mitochondrial membrane potential. (**C**) Detection of mitochondrial ATP content. (**D**, **E**) Qualitative and quantitative detection of mitochondrial calcium ion content. (**F**) Detection of mitochondrial OCR content. (**G**, **H**) Qualitative and quantitative detection of cell apoptosis by flow cytometry. (**I**) Detection of mitochondrial NAD^+ content. (**J**) Transmission electron microscopy (TEM) examination of mitochondrial structure. G1: LPS; G2: BMSCs; G3: OE-miR-20b-BMSCs; G4:SeNPs@CS + OE-miR-20b-BMSCs. ***($P < 0.001$), **($P < 0.01$), *($P < 0.05$)

increased, and the mitochondrial transfer rate between the two cell types is also significantly elevated.

SeNPs@CS synergizes with BMSCs to target and inhibit Th17 expression in alveolar lavage fluid and peripheral blood, thereby exerting anti-inflammatory effects

To further validate at the animal level the synergistic effect of SeNPs@CS and miR-20b-transfected BMSCs in targeting and inhibiting the RORγt/STAT3 pathway, downregulating Th17 expression, and achieving anti-inflammatory effects for the treatment of ALI, we established an ALI model using the cecal ligation method. We collected alveolar lavage fluid and peripheral blood from mice and analyzed Th17 cells using flow cytometry (Fig. 6). As shown in Fig. 6A, B, C, D, E, F, G, and H indicating that in both alveolar lavage fluid and peripheral blood of mice, the proportion of Th17 cells was significantly higher in the Model group compared to the Sham

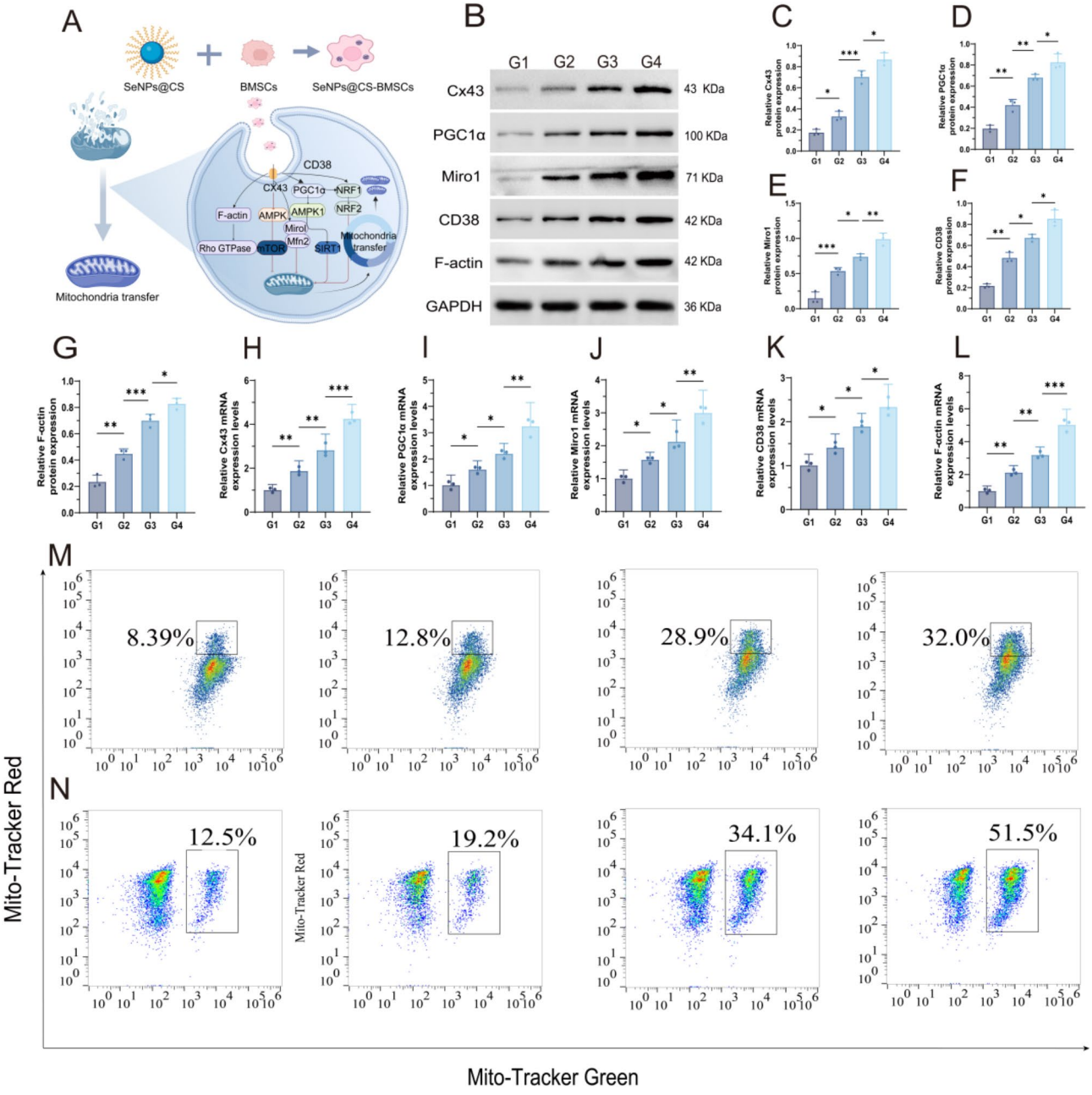

Fig. 5 Detection of the mitochondrial exchange laws. (**A**) Mitochondrial transfer was detected using WB, q-PCR, and flow cytometry. (**B**, **C**, **D**, **E**, **F**, **G**) WB was used for qualitative and quantitative analysis of Cx43, PGC1α, Miro1, CD38, and F-actin. (**H**, **I**, **J**, **K**, **L**) Theexpression levels of Cx43, PGC1α, Miro1, F-actin, and CD38 were determined by q-PCR. (**M**) Flow cytometry was utilized for quantitative analysis of mitochondrial transfer in BMSCs. (**N**)flow cytometry was employed for quantitative assessment of mitochondrial transfer in AECII cells. G1: LPS; G2:BMSCs; G3: OE-miR-20b-BMSCs; G4: SeNPs@CS + OE-miR-20b-BMSCs. ***($P < 0.001$), **($P < 0.01$), *($P < 0.05$)

group. Compared to the BMSCs group, the proportion of Th17 cells was significantly reduced in the OE-miRNA-20b BMSCs group. Additionally, compared to the use of OE-miRNA-20b BMSCs alone, the combination therapy with SeNPs@CS resulted in a noticeable decrease in the proportion of Th17 cells. Furthermore, ELISA was used to detect the expression levels of inflammatory factors in peripheral blood, further supporting the above conclusions (Fig. 6I, J, K, L, M, N, O, and P). These experimental results demonstrate that the therapeutic effect of BMSCs incubated with SeNPs@CS is significantly superior to single treatment components. Additional results further reveal that BMSCs incubated with SeNPs@CS can inhibit the expression of Th17 in bronchoalveolar lavage fluid and peripheral blood, thereby achieving an anti-inflammatory effect.

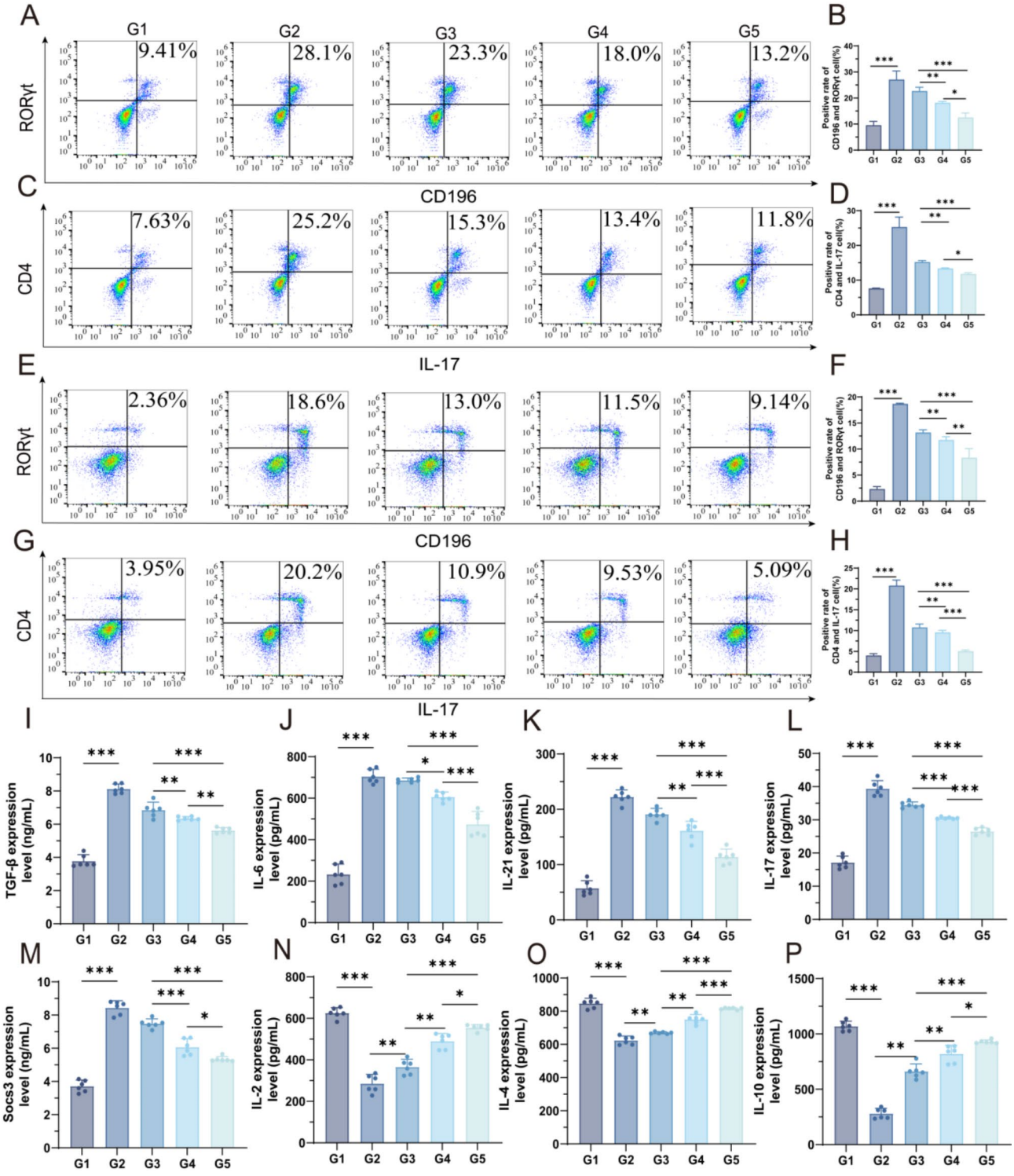

Fig. 6 Flow cytometry and ELISA were used to detect the expression of Th17 and pro/anti-inflammatory factors. (**A**, **B**, **C**, **D**) Flow cytometry detection of Th17 expression in alveolar lavage fluid. (**E**, **F**, **G**, **H**) Flow cytometry detection of Th17 expression in peripheral blood. (**I**, **J**, **K**, **L**, **M**) ELISA detection of pro-inflammatory factor expression in peripheral blood. (**N**, **O**, **P**) ELISA detection of anti-inflammatory factor expression in peripheral blood. G1: Sham; G2: Model; G3: BMSCs; G4: OE-miR-20b-BMSCs; G5: SeNPs@CS + OE-miR-20b-BMSCs. ***(P < 0.001), **(P < 0.01), *(P < 0.05)

Detection of selenoenzymes and mitochondrial transfer-related genes

To further explore the therapeutic mechanism at the animal level (Fig. 7A), We collected lung tissue samples and conducted a series of experimental protocols for examination. Initially, WB was employed to assess the expression levels of RORγt, STAT3, GPX4, TrxR1, TrxR2, as well as mitochondrial transfer-related proteins Cx43, PGC1α, Miro1, and the extracellular enzyme CD38 (Fig. 7B). The results indicated a significant increase in the expression of RORγt and STAT3 in the model group compared to the sham operation group (Sham group), while the expression of GPX4, TrxR1, TrxR2, Cx43, PGC1α, Miro1, and CD38 was significantly reduced. In comparison to the bone marrow mesenchymal stem cells (BMSCs) group, the expression of RORγt and STAT3 was notably decreased in BMSCs treated with SeNPs@CS-OE-miRNA-20b group, whereas the expression of GPX4, TrxR1, TrxR2, Cx43, PGC1α, Miro1, and CD38 was markedly increased. Compared to the OE-miRNA-20b-BMSCs, the SeNPs@CS-OE-miRNA-20b-BMSCs showed a significant decrease in RORγt and STAT3 expression and a significant increase in the expression of GPX4, TrxR1, TrxR2, Cx43, PGC1α, Miro1, and CD38. These findings were further validated by q-PCR results (Fig. 7F, G, H, I, J, K, L, and M). Additionally, oxidative stress indicators such as reactive oxygen species (ROS), superoxide dismutase (SOD) activity, and malondialdehyde (MDA) content in lung tissue were measured using enzyme-linked immunosorbent assay (ELISA). The results revealed a significant increase in ROS levels and MDA content, and a significant decrease in SOD activity in the Model group compared to the Sham group. In contrast, the SeNPs@CS combined with OE-miRNA-20b-treated BMSCs group showed significantly reduced ROS levels and MDA content, and increased SOD activity compared to the BMSCs group (Fig. 7C, D, and E). Subsequently, we removed the lung tissue and examined the lung we/dry (W/D) ratio (Fig. 7N). The results showed that the lung W/D ratio was significantly higher in the model group compared with the Sham group. In the SeNPs@CS combined with OE-miRNA-20b-treated BMSCs group, a significant decrease in the lung W/D ratio compared to the BMSCs group. Furthermore, the survival rate of mice was examined in each group. The survival rate of mice in the Model group was significantly lower compared to the Sham group (Fig. 7O). Compared to the BMSCs group, the survival rate of the SeNPs@CS combined with the OE-miRNA-20b MSCs group was significantly increased. Compared to the OE-miRNA-20b MSCs group, the survival rate of the SeNPs@CS combined with the OE-miRNA-20b MSCs group was significantly increased. These experimental results suggest that BMSCs incubated with SeNPs@CS can effectively deliver healthy mitochondria to the damaged lung tissue, thereby exerting anti-inflammatory and anti-apoptotic effects and prolonging the survival rate of mice.

Pathological and immunohistochemical analysis in animals

Subsequently, the tissues were stained with hematoxylin and eosin (HE) (Fig. 8A and B). The results demonstrated severe alveolar structure damage, and significantly increased inflammatory cell infiltration in the Model group compared to the Sham group. In the SeNPs@CS combined with OE-miRNA-20b-treated BMSCs group, there was a reduction in alveolar structure damage, and decreased inflammatory cell infiltration compared to the BMSCs group. Further, immunohistochemistry was employed to assess the expression of Cx43, GPX4, RORγt, STAT3, and TrxR1 in mouse lung tissue (Fig. 8C, D, E, F, G, and H). Positive expression of Cx43, GPX4, RORγt, STAT3, and TrxR1 proteins was observed as a brown-yellow color. For the three markers GPX4, TrxR1, and Cx43, the Sham group and the SeNPs@CS combined with the OE-miRNA-20b BMSCs group exhibited deeper brown-yellow staining, indicating higher positive expression and protein expression levels. Compared to these two groups, the BMSCs group and the OE-miRNA-20b BMSCs group showed lighter brown-yellow staining, suggesting lower positive expression and protein expression levels. Moreover, compared to the BMSCs group, the Model group demonstrated even lighter brown-yellow staining and reduced positive expression, indicating the lowest protein expression levels. Conversely, the expression patterns of RORγt and STAT3 were opposite to those of GPX4, TrxR1, and Cx43. These findings further support that BMSCs incubated with SeNPs@CS can effectively promote mitochondrial transfer and rapidly achieve the biological effects of selenoenzymes. Animal experiment results further show that BMSCs incubated with SeNPs@CS can, on the one hand, upregulate the expression of miR-20b, thereby inhibiting the activation of the RORγt/STAT3 signaling pathway, further suppressing the differentiation of $CD4^+$ T cells into Th17 cells, and achieving an anti-inflammatory effect. On the other hand, they can deliver healthy mitochondria to the lesion site, achieving exogenous supplementation and ultimately achieving a two-pronged therapeutic approach.

Conclusions

In this study, we employed BMSCs as the primary therapeutic agent for the treatment of ALI. However, the clinical application of BMSCs in ALI therapy is often constrained by their diminished proliferative and differentiation capacities as they age. To address this limitation, we successfully synthesized SeNPs@CS and discovered that co-incubation of BMSCs with SeNPs@CS effectively mitigates the age-related decline in proliferation

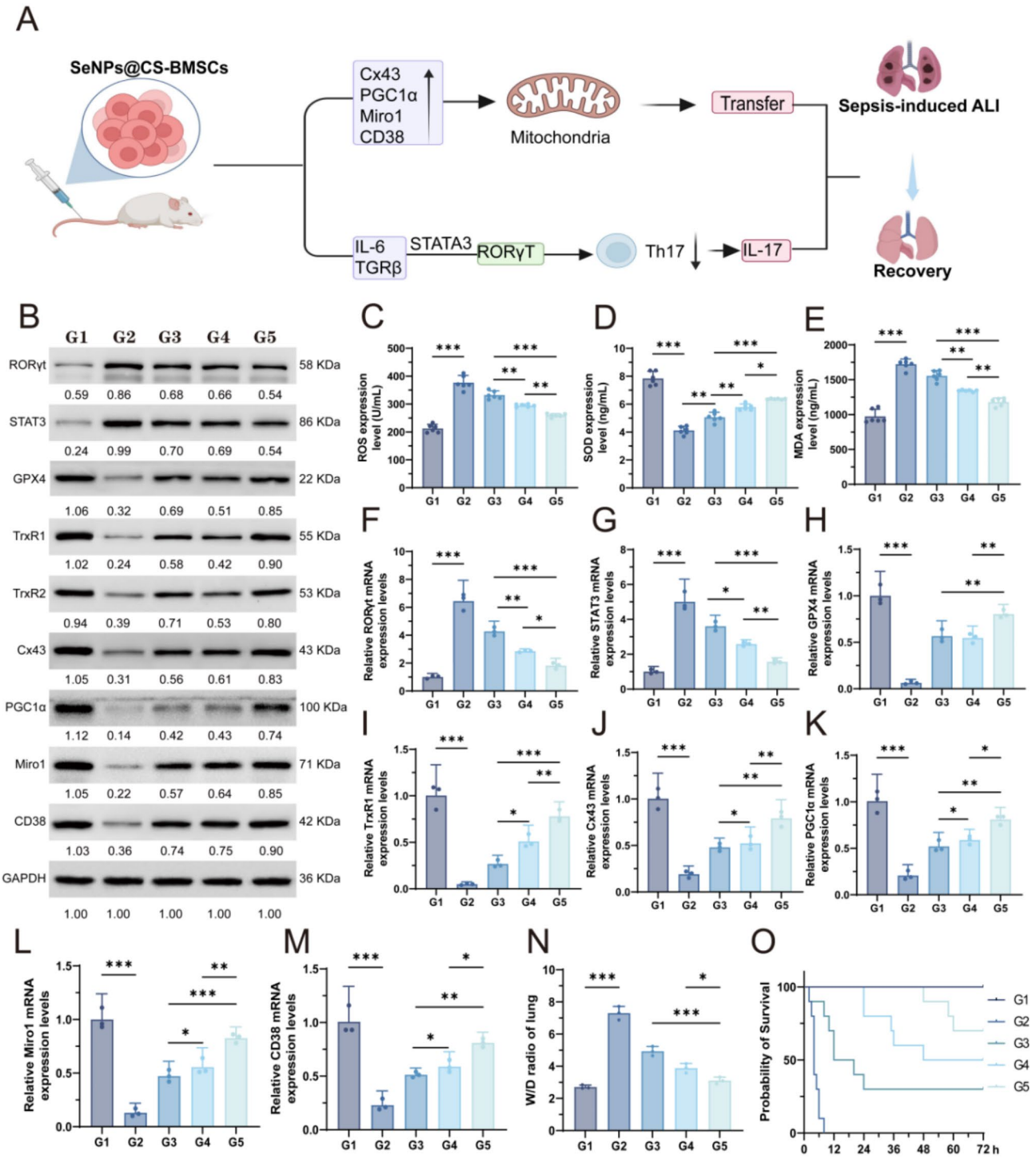

Fig. 7 Explore the therapeutic mechanism in the animals. (**A**) Detection of selenoenzymes and mitochondrial transfer-related genes and proteins in lung tissue. (**B**) WB analysis was conducted to detect the expression levels of RORγt, STAT3, GPX4, TrxR1, TrxR2, Cx43, PGC1α, Miro1, and CD38. (**C**, **D**, **E**) ELISA assay was performed to measure the expression of ROS, SOD, and MDA. (**F**, **G**, **H**, **I**, **J**, **K**, **L**, **M**) q-PCR was used to assess the mRNA levels of RORγt, STAT3, GPX4, TrxR1, Cx43, PGC1α, Miro1, and CD38. (**N**) The wet/dry weight ratio of the lungs was calculated. (**O**) Survival curves were generated to assess the survival rate of mice. G1: Sham; G2: Model; G3: BMSCs; G4: OE-miR-20b-BMSCs; G5: SeNPs@CS + OE-miR-20b-BMSCs. ***($P < 0.001$), **($P < 0.01$), *($P < 0.05$)

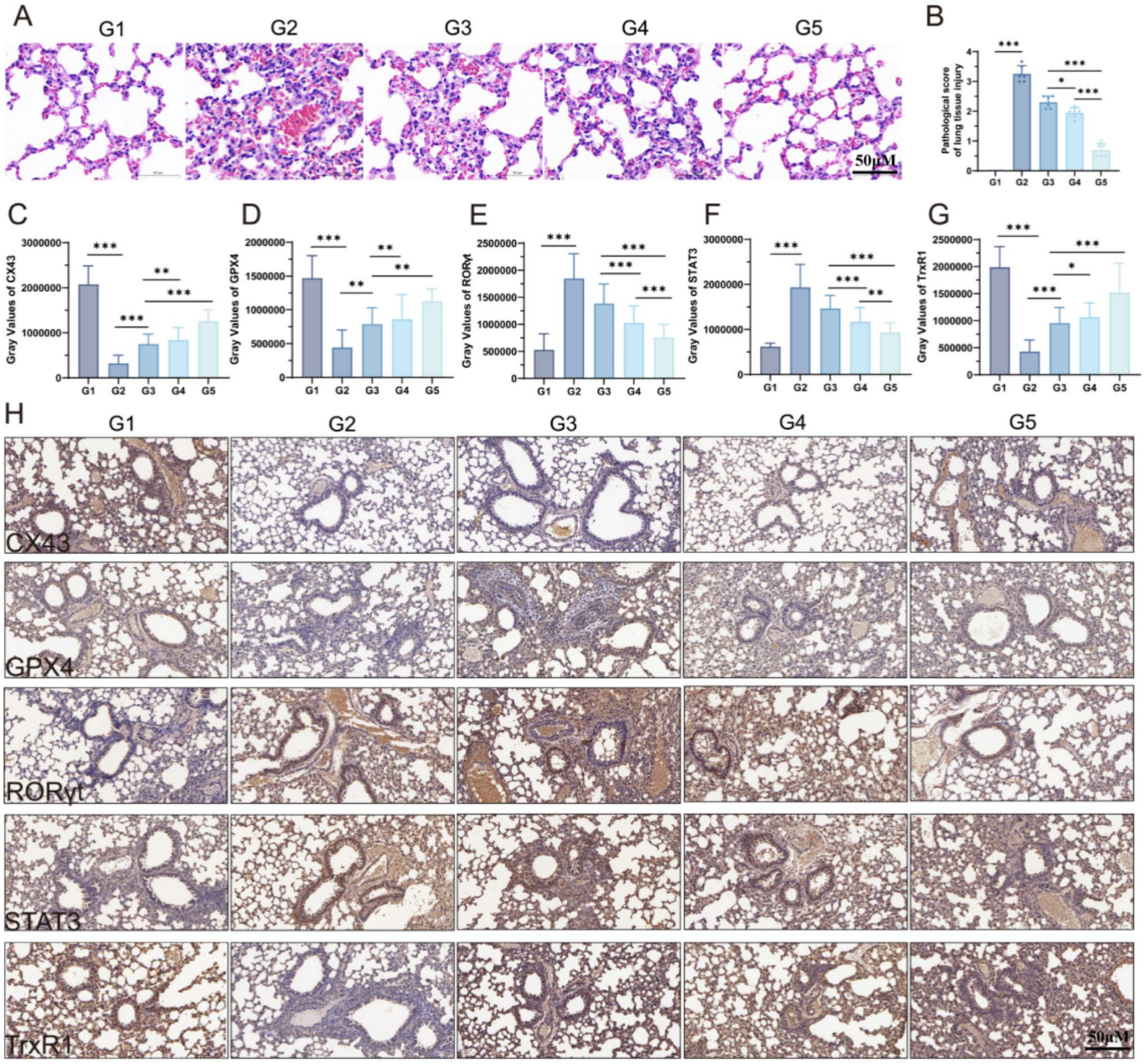

Fig. 8 Pathological histochemical detection in vivo. (**A**, **B**) HE of mouse lung tissue was carried out. (**C**, **D**, **E**, **F**, **G**, **H**) Immunohistochemical detection of Cx43, GPX4, RORγt, STAT3, and TrxR1 expression in mouse lung tissue. G1: Sham; G2: Model; G3: BMSCs; G4: OE-miR-20b-BMSCs; G5: SeNPs@CS + OE-miR-20b-BMSCs. ***($P < 0.001$), **($P < 0.01$), *($P < 0.05$)

and differentiation, thereby enhancing their clinical utility. Experimental findings demonstrated that SeNPs@CS upregulates the expression of miR-20b in BMSCs, which in turn promotes their proliferation and differentiation. Further investigations showed that co-culturing SeNPs@CS-treated BMSCs with $CD4^+$T cells results in the downregulation of Th17 expression by inhibiting the RORγt/STAT3 pathway, thereby reducing oxidative stress and inflammation. Additionally, when SeNPs@CS-treated BMSCs were co-cultured with LPS-induced lung epithelial cells, there was a significant upregulation of proteins associated with mitochondrial transfer, including Cx43, PGC1α, Miro1, and CD38. This was accompanied by an increased rate of mitochondrial exchange between the two cell types, suggesting that healthy mitochondria were transferred from BMSCs to the LPS-induced inflammatory lung epithelial cells, thereby exerting a therapeutic effect. In vivo experiments further corroborated that SeNPs@CS synergistically enhances the proliferative and differentiation capacities of BMSCs, upregulates selenoprotein expression, and reduces oxidative damage and inflammation. The combination of SeNPs@CS and BMSCs downregulates RORγt/STAT3 levels in $CD4^+$ T cells by promoting miR-20b expression, thereby

inhibiting Th17 differentiation and protecting type II alveolar epithelial cells from secondary damage. Moreover, the delivery of healthy mitochondria from BMSCs to damaged lung epithelial cells further underscores the therapeutic potential of this approach. On one hand, the miR-20b-mediated RORγt/STAT3/Th17 axis suppresses Th17 differentiation to achieve an anti-inflammatory effect. On the other hand, a dual repairing mechanism, consisting ofmitochondrial transfer enhancement and selenoprotein activation, allows the exogenous supplementation of healthy mitochondria. By co-incubating SeNPs with BMSCs in vitro, we can pre-activate the stem cells' mitochondrial transfer capaility and anti-inflammatory phenotype, enabling them to function as "super repairers" in vivo and overcome the limitations of traditional stem cell therapies' inconsistent efficacy. Taken together, this study highlights the promising role of SeNPs@CS in enhancing the therapeutic efficacy of BMSCs for ALI, offering a novel strategy to overcome the limitations associated with aged BMSCs in clinical applications.

Materials and methods

Materials

Sodium selenite (Na_2SeO_3, SeIV); Chitosan (≥ 85% deacetylated, average molecular weight = 100,000-300,000gmol^{-1}) was purchased from J&K Scientific Ltd. (Shanghai, China); Fetal Bovine Serum (FSD500); Penicillin-Streptomycin Solution (100X) (C0222) (Beyotime, China); Trypsin (R001100) (Gibco, China); Cell Cryopreservation Medium (C0210B-50 ml); CCK8 Cell Proliferation Assay Kit; MiPure Cell/Tissue miRNA Ki, Oxygen Consumption Rate (OCR) Fluorometric Assay Kit, Enhanced ATP Assay Kit, Fura-2 AM, Mitochondrial Membrane Potential Assay Kit, Dual Luciferase Reporter Gene Assay Kit, Mito-Tracker Green, Mito-Tracker Red CMXRos, riboFECT CP Transfection Kit Prestained Protein Marker II (10–200 kDa); TrxR1 (D1T3D) Rabbit mAb (15140), STAT3 Mouse mAb (9139),TrxR2 Antibody, Connexin 43 Antibody, PGC1a Monoclonal antibody, RORC Polyclonal antibody, Anti-MIRO1 antibody, Anti-CD38 antibody, Anti-F-actin antibody, Western Antibody GAPDH-Loading Control, Goat Anti-Rabbit IgG H&L/HRP, Goat Anti-Mouse IgG H&L/HRP.

Preparation of SeNPs@CS

Prepare a stock solution of chitosan (CS) by dissolving 200 mg of CS in 10 mL of deionized water to a concentration of 20 mg/mL. Store this solution in a refrigerator at 4℃ for later use. Similarly, prepare stock solutions of sodium selenite ($NaSeO_3$) and vitamin C (Vc) by dissolving 173 mg of $NaSeO_3$ and 176 mg of Vc, respectively, in 10 mL of deionized water to a concentration of 100 mM. Store these solutions in a refrigerator at 4℃ as well. Take 1 mL of the CS stock solution and place it in a 25 mL beaker. Add 0.5 mL of the $NaSeO_3$ stock solution and top up with deionized water to 8 mL. Mix the solution well by stirring for 5 min. Then, gradually add 2 mL of Vc to the mixture, drop by drop, while stirring at room temperature overnight. After the reaction is complete, place the reaction solution in a dialysis bag with a molecular weight cutoff of 10,000–20,000 kDa and dialyze for 12–24 h to remove unreacted materials, including CS, $NaSeO_3$, and Vc. The final product is then stored at 4℃.

Characterization of SeNPs@CS

Prepare a solution of SeNPs@CS at an appropriate concentration and measure it using a UV-visible spectrophotometer. Place a drop of SeNPs@CS on a copper grid and allow it to dry completely before observing the morphological structure of SeNPs@CS using TEM. Magnification: 100,000×, operating voltage 200 kV. Place a drop of SeNPs@CS on a silicon wafer and allow it to dry completely before observing the surface morphology of SeNPs@CS using SEM. Test conditions: 5 kV electron beam. Take an appropriate concentration of SeNPs@CS and use a nanoparticle size analyzer to determine the particle size (nm) and zeta potential (mV). Grind and compress CS and SeNPs@CS with potassium bromide in an agate mortar, and obtain infrared spectra by scanning with a Fourier transform infrared spectrometer in the range of 4000–400 cm^{-1}. Use XPS to irradiate the sample and analyze the chemical and electronic states of selenium in SeNPs@CS.

GEO database

In this study, the dataset GSE9664 was downloaded from the GEO database (https://www.ncbi.nlm.nih.gov/geo/) and annotated based on the GPL6127 platform. The GSE9664 dataset originates from a cellular-aged model of human bone marrow mesenchymal stem cells (MSC). Differential microRNA (miRNA) expression between early and senescent passages was analyzed using the limma package in R. Differentially expressed genes (DEGs) were identified using the criteria of $P < 0.05$ and $|logFC| \geq 0.5$. Volcano plots and clustering heatmaps were generated using the ggplot2 and pheatmap packages, respectively, for visualization.

Cell culture

Cells were cultured in a complete medium, maintained at 37℃ in a cell culture incubator with 95% air and 5% CO_2. When the cell culture density reached over 80%, the cells were digested with 1 ml of 0.25% trypsin for 1 min. Once the cells became rounded and detached, digestion was terminated by adding 5 ml of complete medium, followed by subculturing.

Method for constructing an aged BMSC model

To induce aging in BMSCs, hydrogen peroxide (H_2O_2) was used. Specifically, BMSCs were treated with 200 μmol/L H_2O_2 for 2 h, followed by the detection of cell proliferation activity.

Construction of inflammatory, OE-miRNA-20b-5p, and OE-RORγt cell models in vitro

Alveolar type II epithelial cells were stimulated with lipopolysaccharide (LPS) at a concentration of 1 μg/mL. Bone marrow stromal cells (BMSCs) were selected as the study subjects to construct a miRNA-20b-5p mimic and negative control (NC) transfection system. The miRNA-20b-5p sequence was obtained from NCBI, and based on this sequence, miRNA-20b-5p mimic and mimic NC sequences were designed (synthesized by Shanghai Sangon Biotech Co., Ltd.). Cells were transfected according to the reagent instructions. $CD4^+$ T cells were chosen as the research subjects to construct an OE-RORγt lentiviral overexpression vector (synthesized by Shanghai Sangon Biotech Co., Ltd.), using the pLV-Puro vector. The CDS sequence of the RORγt gene was obtained from NCBI with the accession number > NM_001293734.1:166–1653. RORγt was inserted into the vector to construct the pLV-Puro-OE-RORγt plasmid. After construction, it was packaged into a lentivirus using a lentiviral packaging system. Once the constructed lentiviral expression vector was obtained, it could be transfected into cells.

miRNA-20b-5p
CAAAGUGCUCAUAGUGCAGGUAG

mimics NC
UCACAACCUCCUAGAAAGAGUAGA
UCUACUCUUUCUAGGAGGUUGUGA

Animal model development and therapeutic intervention

C57BL/6J mice underwent cecal ligation puncture (CLP)-induced acute lung injury modeling. The surgical protocol involved mid-cecal ligation (50% cecal length) followed by transmural perforation using 20G needle at the anti-mesenteric border to achieve controlled fecal extrusion. Postoperative treatment comprised systemic delivery of bone marrow mesenchymal stem cells (BMSCs, 1×10^6 cells/mL) through 4-hour interval caudal vein injections (0.1 mL/dose). Terminal tissue collection and histopathological evaluation were performed 72 h post-intervention.

Cell proliferation assessment via CCK-8

Log-phase cultures were plated in 96-well microplates (5×10^3cells/well) with quadruplicate technical replicates per condition. Following 6 h stabilization in 5% CO_2 at 37 °C, experimental treatments were administered. At 24 h post-treatment, CCK-8 reagent (10 μL/well) was introduced 2 h prior to absorbance measurement at 450 nm using multimode microplate reader.

Th17 lymphocyte profiling by flow cytometry

Single-cell suspensions (1×10^6 cells/mL) from trypsinized cultures or bronchoalveolar lavage specimens were prepared through sequential centrifugation (800 rpm × 5 min) and PBS washing. Fluorochrome-conjugated antibodies (10 μL/test) were incubated with cell aliquots (5×10^5 cells in 50 μL) under light-protected conditions (RT, 60 min). Post-staining procedures included two-cycle PBS washing and final resuspension in 300 μL PBS for cytometric analysis.

Analysis of selenium enzyme and mitochondrial transfer-related gene expression

Total RNA isolation from alveolar macrophages/pulmonary tissues was performed using Trizol reagent (Takara, Japan). Reverse transcription employed PrimeScript RT Master Mix (Takara) followed by quantitative PCR on CFX Connect™ system (Bio-Rad) with SYBR Premix Ex Taq II. Gene expression normalization utilized dual reference genes (GAPDH/U6) through $2^{-\Delta\Delta Ct}$ method.

Detection of mitochondrial membrane potential with TMRE kit

TMRE-based membrane potential detection: Pre-treated cells (1×10^6/well) were stained with TMRE working solution (1 mL, 37 °C × 30 min). Post-staining visualization employed fluorescence microscopy (Ex/Em: 550/575 nm).

Detection of intracellular Ca2+ content

Cells in the logarithmic growth phase were seeded in a 6-well plate at a density of 1×10^6 cells per well. The cells in each group were treated according to the experimental groupings and cultured in a cell incubator at 37 °C with 5% CO_2 until the cell density reached approximately 80%. The commonly used concentration of Fura-2 AM ranges from 0.5 to 5 μM. Typically, the cells were incubated with a suitable solution containing 2 μM Fura-2 AM at 37°C for 40 min to complete the loading of the fluorescent probe. After incubation at 37°C, the supernatant was aspirated, and the cells were washed twice before observation under a fluorescence microscope or confocal laser scanning microscope.

Detection of mitochondrial distribution in cells using Mito-Tracker green fluorescence microscopy

Before use, the Mito-Tracker Green working solution needs to be pre-incubated at 37℃. Remove the cell culture medium, add the prepared and pre-incubated

Mito-Tracker Green, and incubate with the cells at 37℃ for 15 min. Then, stain the cell nuclei with Hoechst 33,342 for 10 min. Remove the staining solution and add fresh cell culture medium pre-incubated at 37℃. Subsequently, observe under a fluorescence microscope.

Apoptosis quantification via Annexin V/PI

Treated cells were harvested through enzymatic detachment and dual staining with FITC-Annexin V (5 μL) and propidium iodide (5 μL) in Annexin binding buffer. Flow cytometric acquisition was completed within 60 min post-staining.

Western blot experiment

Cellular proteins were lysed with RIPA buffer (Beyotime, Shanghai, China) followed by quantitative analysis using a BCA assay kit (NCM Biotech, China). Equal aliquots of protein extracts (40 μg/lane) underwent electrophoretic separation through SDS-PAGE systems and subsequent electrotransfer onto PVDF membranes. Membranes were initially blocked with 5% skim milk-TTBS solution for 2 h at ambient temperature prior to sequential immunoreactions: primary antibody incubation (specific concentrations/durations based on antibody specifications) followed by 2 h exposure to HRP-conjugated secondary antibodies at room temperature. Protein signals were ultimately captured through chemiluminescent detection using the JP-K6000 imaging platform.

Dual luciferase reporter assay

The miRNA-20b-5p sequence was obtained from NCBI, and a luciferase reporter vector was designed based on the predicted binding site. The pmir-GLO was used to construct a vector incorporating both the firefly luciferase (FLuc) as the main reporter gene and the Renilla luciferase (RLuc) as the internal reference, with TK serving as the promoter. The completed dual-luciferase reporter vector plasmid was provided by Shanghai Sangon Biotech Co., Ltd. The plasmid carrying the luciferase-labeled target gene and the internal reference gene plasmid were co-transfected with HEK-293T cells for 48 h according to grouping. The ratio of the plasmid carrying the target gene to the plasmid carrying the internal reference was 50:1. After fully mixing the reporter gene cell lysate, the reporter gene cell lysate was added according to the instructions. After sufficient lysis, the supernatant was taken for determination.

HE staining of lung tissue sections

Formalin-fixed lung tissues underwent paraffin embedding and 4 μm sectioning. Nuclear/cytoplasmic differentiation is achieved through hematoxylin-eosin sequential staining with acid alcohol differentiation.

Immunohistochemical detection of lung tissue

Mouse lung tissue was removed from the fixative solution and dehydrated through a gradient of ethanol in a dehydrator. The melted paraffin was placed into an embedding frame, and the embedded paraffin block was then placed in a refrigerator at 4℃ for shaping. The shaping time was determined according to subsequent experiments. The prepared sections were clamped with small tweezers and placed into a constant temperature water bath at 45℃ to spread out. Once the sections flattened out, they were retrieved from the water with a slide glass and allowed to dry naturally before being dried in an oven at 37℃. Further processing involved dewaxing and hydration of the sections, followed by antigen retrieval. Antibody hybridization was performed using endogenous peroxidase blocking, and further staining was done with hematoxylin. The sections were then dehydrated and cleared, finally mounted and photographed. Relevant proteins included RORγt, STAT3, GPX4, TrxR1, and Cx43.

Data analysis

Experimental data were processed using GraphPad Prism 9.5.1 and ImageJ. Data normality was confirmed prior to parametric testing (Student's t-test for pairwise comparisons; one-way ANOVA with post-hoc analysis for multi-group). Graphical representations prepared in Adobe Illustrator 2023. Significance thresholds: $^{*}P < 0.05$, $^{**}P < 0.01$, $^{***}P < 0.001$.

Supplementary Information

The online version contains supplementary material available at https://doi.org/10.1186/s12951-025-03312-2.

Supplementary Material 1

Acknowledgements

Not applicable.

Author contributions

WJG and FZZ contributed equally to this work. WJG, FZZ, HYY, and TC conceived and designed this study; WJG and FZZ contributed to the major experiments; WH, MGZ, and HYH provided help in the experiments; WJG and FZZ drafted the manuscript and all author revised the manuscript. All authors read and approved the final manuscript.

Funding

This work was supported by the National Natural Science Foundation of China (82072232), Funding by Science and Technology Projects in Guangzhou (2025A03J4248, 2025A03J3472).

Data availability

No datasets were generated or analysed during the current study.

Declarations

Ethics approval and consent to participate

All animal experimental care and operating procedures were performed in accordance with the Guidelines for Care and Use of Laboratory Animals and approved by by the the Animal Ethical and Welfare Committee (Approval number: IACUC-MIS2023075).

Consent for publication
Not applicable.

Competing interests
The authors declare no competing interests.

Received: 22 February 2025 / Accepted: 9 March 2025
Published online: 20 March 2025

References

1. Ericson JE, Agthe AG, Weitkamp JH. Late-Onset sepsis: epidemiology, microbiology, and controversies in practice. Clin Perinatol. 2025;52(1):33–45.
2. Xu JQ, Zhang WY, Fu JJ, Fang XZ, Gao CG, Li C, et al. Viral sepsis: diagnosis, clinical features, pathogenesis, and clinical considerations. Mil Med Res. 2024;11(1):78.
3. Prescott HC, Angus DC. Enhancing recovery from sepsis: A review. JAMA. 2018;319(1):62–75.
4. Rudd KE, Johnson SC, Agesa KM, Shackelford KA, Tsoi D, Kievlan DR, et al. Global, regional, and National sepsis incidence and mortality, 1990–2017: analysis for the global burden of disease study. Lancet. 2020;395(10219):200–11.
5. Sun B, Lei M, Zhang J, Kang H, Liu H, Zhou F. Acute lung injury caused by sepsis: how does it happen? Front Med (Lausanne). 2023;10:1289194.
6. Wu C, Li H, Zhang P, Tian C, Luo J, Zhang W, et al. Lymphatic flow: A potential target in Sepsis-Associated acute lung injury. J Inflamm Res. 2020;13:961–8.
7. Li G, Zhang L, Han N, Zhang K, Li H. Increased Th17 and Th22 cell percentages predict acute lung injury in patients with Sepsis. Lung. 2020;198(4):687–93.
8. Chen J, Liu Z, Chen J, Shen M, Zhu J. Level changes and clinical significance of peripheral blood Th22 and Th17 cells in septic patients with acute lung injury. Panminerva Med. 2022;64(3):401–2.
9. Li N, Liu B, Xiong R, Li G, Wang B, Geng Q. HDAC3 deficiency protects against acute lung injury by maintaining epithelial barrier integrity through preserving mitochondrial quality control. Redox Biol. 2023;63:102746.
10. Huang W, Wen L, Tian H, Jiang J, Liu M, Ye Y, et al. Self-Propelled proteomotors with active Cell-Free MtDNA clearance for enhanced therapy of Sepsis-Associated acute lung injury. Adv Sci (Weinh). 2023;10(27):e2301635.
11. Wang H, Sun X, Lu Q, Zemskov EA, Yegambaram M, Wu X, et al. The mitochondrial redistribution of eNOS is involved in lipopolysaccharide induced inflammasome activation during acute lung injury. Redox Biol. 2021;41:101878.
12. Tang X, Zhong L, Tian X, Zou Y, Hu S, Liu J, et al. RUNX1 promotes mitophagy and alleviates pulmonary inflammation during acute lung injury. Signal Transduct Target Ther. 2023;8(1):288.
13. Ye L, Gao Y, Mok SWF, Liao W, Wang Y, Chen C, et al. Modulation of alveolar macrophage and mitochondrial fitness by medicinal plant-derived nanovesicles to mitigate acute lung injury and viral pneumonia. J Nanobiotechnol. 2024;22(1):190.
14. Amaral AC, Amado VM. Fluid-management strategies in acute lung injury. N Engl J Med. 2006;355(11):1175. author reply 6.
15. Mokra D, Mikolka P, Kosutova P, Mokry J. Corticosteroids in acute lung injury: the dilemma continues. Int J Mol Sci. 2019;20(19).
16. Brochard L, Slutsky A, Pesenti A. Mechanical ventilation to minimize progression of lung injury in acute respiratory failure. Am J Respir Crit Care Med. 2017;195(4):438–42.
17. Zhu M, Tang X, Xu J, Gong Y. Identification of HK3 as a promising Immunomodulatory and prognostic target in sepsis-induced acute lung injury. Biochem Biophys Res Commun. 2024;706:149759.
18. Gasperino J, Kvetan V. Acute lung injury and nutritional support. Crit Care Med. 2006;34(4):1265–7.
19. van Kaam AH. Optimal strategies of mechanical ventilation: can we avoid or reduce lung. Injury? Neonatology. 2024;121(5):570–5.
20. Yang L, Cao J, Du Y, Zhang X, Hong W, Peng B, et al. Initial IL-10 production dominates the therapy of mesenchymal stem cell scaffold in spinal cord injury. Theranostics. 2024;14(2):879–91.
21. Wang G, Ma X, Huang W, Wang S, Lou A, Wang J, et al. Macrophage biomimetic nanoparticle-targeted functional extracellular vesicle micro-RNAs revealed via multiomics analysis alleviate sepsis-induced acute lung injury. J Nanobiotechnol. 2024;22(1):362.
22. Chen J, Ma S, Luo B, Hao H, Li Y, Yang H, et al. Human umbilical cord mesenchymal stromal cell small extracellular vesicle transfer of microRNA-223-3p to lung epithelial cells attenuates inflammation in acute lung injury in mice. J Nanobiotechnol. 2023;21(1):295.
23. Ding Z, Yan Z, Yuan X, Tian G, Wu J, Fu L, et al. Apoptotic extracellular vesicles derived from hypoxia-preconditioned mesenchymal stem cells within a modified gelatine hydrogel promote osteochondral regeneration by enhancing stem cell activity and regulating immunity. J Nanobiotechnol. 2024;22(1):74.
24. Lei T, Li C, Liu Y, Cui Z, Deng S, Cao J, et al. Microfluidics-enabled mesenchymal stem cell derived neuron like cell membrane coated nanoparticles inhibit inflammation and apoptosis for Parkinson's disease. J Nanobiotechnol. 2024;22(1):370.
25. Figueroa-Valdes AI, Luz-Crawford P, Herrera-Luna Y, Georges-Calderon N, Garcia C, Tobar HE, et al. Clinical-grade extracellular vesicles derived from umbilical cord mesenchymal stromal cells: preclinical development and first-in-human intra-articular validation as therapeutics for knee osteoarthritis. J Nanobiotechnol. 2025;23(1):13.
26. Wang D, Xu L, Liu Y, Wang C, Qi S, Li Z et al. Role of mesenchymal stem cells in sepsis and their therapeutic potential in sepsis–associated myopathy (Review). Int J Mol Med. 2024;54(5).
27. Liu L, Zhou N, Fu S, Wang L, Liu Y, Fu C, et al. Endothelial cell-derived exosomes trigger a positive feedback loop in osteogenesis-angiogenesis coupling via upregulating zinc finger and BTB domain containing 16 in bone marrow mesenchymal stem cell. J Nanobiotechnol. 2024;22(1):721.
28. Peng X, Zhou X, Yin Y, Luo B, Liu Y, Yang C. Inflammatory microenvironment accelerates bone marrow mesenchymal stem cell aging. Front Bioeng Biotechnol. 2022;10:870324.
29. You Y, Chang Y, Pan S, Bu Q, Ling J, He W, et al. Cleavage of homonuclear Chalcogen-Chalcogen bonds in a hybrid platform in response to X-Ray radiation potentiates tumor radiochemotherapy. Angew Chem Int Ed Engl. 2025;64(1):e202412922.
30. Chen M, Wang J, Cai F, Guo J, Qin X, Zhang H, et al. Chirality-driven strong thioredoxin reductase Inhibition. Biomaterials. 2024;311:122705.
31. Tian Y, Sun D, Liu N, Zhao J, Zhao T, Liu X, et al. Biomimetic mesenchymal stem cell membrane-coated nanoparticle delivery of MKP5 inhibits hepatic fibrosis through the IRE/XBP1 pathway. J Nanobiotechnol. 2024;22(1):741.
32. Lu L, Quan L, Li J, Yuan J, Nie X, Huang X, et al. Bioengineered stem cell membrane functionalized nanoparticles combine anti-inflammatory and antimicrobial properties for sepsis treatment. J Nanobiotechnol. 2023;21(1):170.
33. Bai S, Zhang M, Tang S, Li M, Wu R, Wan S et al. Effects and impact of selenium on human health, A review. Molecules. 2024;30(1).
34. Schoenmakers E, Chatterjee K. Human disorders affecting the selenocysteine incorporation pathway cause systemic Selenoprotein deficiency. Antioxid Redox Signal. 2020;33(7):481–97.
35. Xie B, Zeng D, Yang M, Tang Z, He L, Chen T. Translational selenium nanoparticles to attenuate allergic dermatitis through Nrf2-Keap1-Driven activation of selenoproteins. ACS Nano. 2023;17(14):14053–68.
36. Rao S, Lin Y, Lin R, Liu J, Wang H, Hu W, et al. Traditional Chinese medicine active ingredients-based selenium nanoparticles regulate antioxidant selenoproteins for spinal cord injury treatment. J Nanobiotechnol. 2022;20(1):278.
37. Chen C, Ma J, Duan S, Xue M, Yang Z, Ma Z, et al. Mitigation of ischemia/reperfusion injury via selenium nanoparticles: suppression of STAT1 to inhibit cardiomyocyte oxidative stress and inflammation. Biomaterials. 2025;318:123119.
38. Liu P, Liu X, Wu Z, Shen K, Li Z, Li X, et al. Size effect-based improved antioxidant activity of selenium nanoparticles regulating Anti-PI3K-mTOR and Ras-MEK pathways for treating spinal cord injury to avoid hormone shock-induced immunosuppression. J Nanobiotechnol. 2025;23(1):17.
39. Xue Q, Lai H, Zhang H, Li G, Pi F, Wu Q, et al. Selenium attenuates radiation colitis by regulating cGAS-STING signaling. Adv Sci (Weinh). 2024;11(44):e2403918.
40. Li Y, Liu T, Zheng R, Lai J, Su J, Li J, et al. Translational selenium nanoparticles boost GPx1 activation to reverse HAdV-14 virus-induced oxidative damage. Bioact Mater. 2024;38:276–91.
41. Zuo Z, Luo M, Liu Z, Liu T, Wang X, Huang X, et al. Selenium nanoparticles alleviate renal ischemia/reperfusion injury by inhibiting ferritinophagy via the XBP1/NCOA4 pathway. Cell Commun Signal. 2024;22(1):376.
42. Qin X, Guo J, Li H, He H, Cai F, Chen X et al. Selenium electrophilic center responsive to biological Electron donors for efficient chemotherapy. Adv Sci (Weinh). 2025:e2412062. https://doi.org/10.1002/advs.202412062. Epub ahead of print.
43. Yu Y, Wang Y, Zhang J, Bu Q, Jiang D, Jiang Y, et al. Anaerobic probiotics-in situ se nanoradiosensitizers selectively anchor to tumor with immuno-regulations for robust cancer radio-immunotherapy. Biomaterials. 2025;318:123117.

44. Qiao R, Yuan Z, Yang M, Tang Z, He L, Chen T. Selenium-Doped nanoheterojunctions for highly efficient Cancer radiosensitization. Adv Sci (Weinh). 2024;11(29):e2402039.
45. Fatima S, Alfrayh R, Alrashed M, Alsobaie S, Ahmad R, Mahmood A. Selenium nanoparticles by moderating oxidative stress promote differentiation of mesenchymal stem cells to osteoblasts. Int J Nanomed. 2021;16:331–43.
46. Zhang S, Zhao X, Xue Y, Wang X, Chen XL. Advances in nanomaterial-targeted treatment of acute lung injury after burns. J Nanobiotechnol. 2024;22(1):342.
47. Chi X, Jin W, Zhao X, Xie T, Shao J, Bai X, et al. RORgammat expression in mature T(H)17 cells safeguards their lineage specification by inhibiting conversion to T(H)2 cells. Sci Adv. 2022;8(34):eabn7774.
48. Nurieva R, Yang XO, Martinez G, Zhang Y, Panopoulos AD, Ma L, et al. Essential autocrine regulation by IL-21 in the generation of inflammatory T cells. Nature. 2007;448(7152):480–3.
49. Supasai S, Adamo AM, Mathieu P, Marino RC, Hellmers AC, Cremonini E, et al. Gestational zinc deficiency impairs brain astrogliogenesis in rats through multistep alterations of the JAK/STAT3 signaling pathway. Redox Biol. 2021;44:102017.
50. Xia H, Wang F, Wang M, Wang J, Sun S, Chen M, et al. Maresin1 ameliorates acute lung injury induced by sepsis through regulating Th17/Treg balance. Life Sci. 2020;254:117773.
51. Song X, Chen Y, Zhao G, Sun H, Che H, Leng X. Effect of molecular weight of Chitosan and its oligosaccharides on antitumor activities of Chitosan-selenium nanoparticles. Carbohydr Polym. 2020;231:115689.
52. Ingold I, Berndt C, Schmitt S, Doll S, Poschmann G, Buday K, et al. Selenium utilization by GPX4 is required to prevent Hydroperoxide-Induced ferroptosis. Cell. 2018;172(3):409–e42221.
53. Prasad CB, Oo A, Liu Y, Qiu Z, Zhong Y, Li N, et al. The thioredoxin system determines CHK1 inhibitor sensitivity via redox-mediated regulation of ribonucleotide reductase activity. Nat Commun. 2024;15(1):4667.

Publisher's note